Cement and Concrete Research 42 (2012) 377–383

Contents lists available at SciVerse ScienceDirect

Cement and Concrete Research

journal homepage: http://ees.elsevier.com/CEMCON/default.asp

Density and water content of nanoscale solid C–S–H formed in alkali-activated slag (AAS) paste and implications for chemical shrinkage

Jeffrey J. Thomas [a,*], Andrew J. Allen [b], Hamlin M. Jennings [c]

[a] Schlumberger-Doll Research, Cambridge, MA 02139, USA
[b] National Institute of Standards and Technology, Gaithersburg, MD 20899, USA
[c] CSHub, Department of Civil and Environmental Engineering, Massachusetts Institute of Technology, Cambridge, MA 02139, USA

ARTICLE INFO

Article history:
Received 16 February 2011
Accepted 7 November 2011

Keywords:
(B) Calcium–Silicate–Hydrate (C–S–H)
(D) Alkali Activated Cement
(D) Granulated Blast- Furnace Slag

ABSTRACT

Alkali-activated slag (AAS) paste was analyzed using small-angle neutron scattering (SANS). The scattering response indicates that the microstructure consists of a uniform matrix of hydration product with a high surface area studded with unhydrated cores of slag particles. In contrast with portland cement paste, no surface fractal scattering regime was detected, and elevated temperature curing (at 60 °C) had no detectable effect on the microstructure at any length scale studied. The specific surface area of the AAS pastes is about 25% higher than that of a portland cement paste cured under the same conditions. The composition and mass density of the nanoscale solid C–S–H phase formed in the AAS paste was determined using a previously developed neutron scattering method, in conjunction with a hydration model. The result $((CaO)_{0.99}–SiO_2–(Al_2O_3)_{0.06}–(H_2O)_{0.97}$, $d = (2.73 \pm 0.02)$ g/cm^3) is significantly lower in calcium and in water as compared to portland cement or pure tricalcium silicate paste. These values were used to calculate the chemical shrinkage that would result from complete hydration of the AAS paste. The result, (12.2 ± 1.5) cm^3 of volumetric shrinkage per 100 g of unhydrated cement, is about twice the amount of chemical shrinkage exhibited by normal cement pastes.

1. Introduction

Ground granulated blast furnace slag is widely used as a cementing material, most commonly as a blend with portland cement where it provides environmental advantages associated with reduced portland cement use (hence, reduced CO_2 emissions associated with cement manufacture) and can improve the long-term properties of the concrete. When used in this way, the high pH of the cement pore solution activates the slag, allowing it to hydrate. Alkali-activated slag (AAS) paste or concrete made from pure slag has been widely studied, both for its commercial potential and as a model system for understanding the hydration of slag within blended cement [1-3]. In the latter case, a chemical activator must be added to raise the pH, most commonly sodium hydroxide or sodium silicate.

There are several potential advantages to the use of AAS concrete, including high rate of strength development, low permeability, high resistance to chemical attack, and a lower rate of heat release than portland cement. In addition, the degree of activation can be varied widely by adjusting the activator type and concentration, providing the potential for controlled setting under a wide range of temperatures. Disadvantages of AAS concrete include difficulty in maintaining early workability [4], a greater amount of autogenous and drying shrinkage [5-7], and a tendency to crack during curing [5,8]. These negative effects can be ameliorated somewhat through the use of shrinkage reducing admixtures [9,10,4]. The greater amount of shinkage has been attributed to the formation of a pore structure with a large proportion of mesopores that create large capillary stresses as they empty [11].

It is well established that the main hydration product formed by activated slag hydration is a calcium silicate hydrate (C–S–H[1]) phase with a rather low calcia to silica molar ratio (C/S) that is typically close to 1. This C–S–H phase also has a non-negligible degree of substitution of alumimum for silicon, with alumina to silica ratios (A/S) typically close to 0.1. For convenience, this aluminum-containing phase will continue to be abbreviated as C–S–H in this paper. Richardson et al. [12] proposed a general model in which aluminum substitutes for silicon at the bridging sites of the drierketten chains, and this model is supported by NMR work conducted by Wang and Scrivener [13]. Hydration of slag also sometimes produces smaller amounts of other hydration products. The only one of these that occurs in significant quantities is a hydrotalcite-type phase. Based on discussions in the literature [14,15] we assume a composition of M_5AH_{13} for this phase. Calcium hydroxide (CH), which is a significant product of

* Corresponding author.
E-mail address: jthomas39@slb.com (J.J. Thomas).

[1] Cement chemistry notation: C=CaO, S=SiO_2, H=H_2O, A=Al_2O_3, M=MgO, F=Fe_2O_3, $\bar{S}$=SO_3.

0008-8846/$ – see front matter © 2011 Elsevier Ltd. All rights reserved.
doi:10.1016/j.cemconres.2011.11.003

cement hydration, does not form due to the lower C/S of the slag. Recently, Chen and Brouwers [15] developed a hydration model for AAS that predicts the quantities of the hydration products and the stoichiometry of the C–S–H phase from the slag composition. This model is utilized in the present work and is discussed in more detail later.

The primary purpose of the present study was to calculate the molar water to silica ratio (H/S) and associated mass density of the solid nanoscale C–S–H phase that forms in AAS paste, using a previously developed method based on small-angle neutron scattering (SANS) measurements in various fluids [16]. This technique can also detect the presence of a secondary nanoscale solid phase, provided that it is crystalline and contains some H_2O; for example, this method can quantify the presence of nanoscale CH in portland cement and C_3S pastes. The present results indicate that hydrotalcite is present as a secondary phase at length scales greater than about 10 nm in the AAS pastes. However, as is the case with CH in OPC paste, the hydrotalcite only makes a significant contribution to the observed scattering if its contrast is enhanced by deuterated fluid exchange. Based on the composition and density for solid C–S–H, the chemical shrinkage that occurs on hydration can be estimated, and this is discussed. Other results obtained from the SANS measurements, including the specific surface area and the general nanostructure of the pastes, are also discussed.

2. Experimental

A commercial Grade 120 ground granulated blast furnace slag (NewCem, Lafarge Cement [17], Joppa, IL) was used; the density of the slag is 2.90 g/cm^3 and the Blaine surface area is 584 m^2/kg. The average particle size for this brand of slag is just over 10 μm. The oxide composition of the batch of slag used here was measured by the manufacturer using X-ray fluorescence, with the exception of the sulfur, which was measured by titration (see Table 1, first data column). The values are the average of approximately 30 measurements conducted over a period of 1 month and the uncertainties are the standard deviations of these measurements. Following the procedure of Chen and Brouwers [15], the compositions of the main oxide components (including the SiO_2 in the activator) are converted to mole percent and normalized to a total of 100%, for input into the stoichiometric model (Table 1, second data column).

The slag was activated with a commercial liquid sodium silicate solution (STAR, PQ Chemical) into which additional NaOH was dissolved to reach a SiO_2/Na_2O mass ratio of 1.76. Prior to mixing, the solution was diluted with water so that at the selected water/slag mass ratio of 0.45 the activator amounts were (by mass of slag) 2.13% Na_2O and 3.75% SiO_2. After mixing for 2 minutes by hand, the pastes were cured for 24 h in sealed plastic cups at either 20 °C or 60 °C. They were then demolded and stored under a small excess of water thereafter at the same temperature. At the time of testing, specimens cured at 20 °C were 28 days and 90 days old; one paste cured at 60°C was 8 days old. A few days before the SANS experiment, thin (0.5 mm thick) coupons were cut from each paste specimen using a water-lubricated wafering saw. One coupon of the paste cured for 28 days at 20 °C was submerged in methanol for 72 h before the SANS measurements to exchange the pore fluid. The methanol was refreshed twice to ensure complete replacement of H_2O in the pore system with methanol.

Table 1
Oxide compositions of the ground slag and of the AAS paste, see text for details.

Oxide	mass%[a]	mole%[b]
CaO	39.7(3)[c]	40.3(3)
SiO_2	35.4(3)	37.1(2)
Al_2O_3	10.3(2)	5.7(1)
MgO	10.9(1)	15.4(2)
SO_3	1.90(23)	1.3(2)
Fe_2O_3	0.5(2)	0.18(6)
Na_2O	0.25(3)	-
Total	99.09	100
C/S (mole)	1.20	1.09
A/S (mole)	0.17	0.16

[a] Of the ground slag, as reported by the supplier.
[b] Of the AAS (includes SiO_2 in activator), normalized to 100%.
[c] Numbers in parentheses are standard deviation uncertainties in least significant digits.

SANS measurements were performed at the NIST Center for Neutron Research using the NIST/NSF NG3 30-m SANS instrument with a neutron wavelength of 0.8 nm. The neutron beam diameter was 6.35 mm. By varying the sample-to-detector distance, data for each specimen were obtained over a magnitude range of scattering vector of $0.02<q<3.0$ nm^{-1}, where $q=4\pi\sin(\varphi/2)/\lambda$, φ is the angle of scatter, and λ is the neutron wavelength. A subset of the specimens was also measured using the BT-5 ultrasmall-angle neutron scattering (USANS) instrument, which extended the q-range down to approximately 0.0008 nm^{-1}. With small-angle scattering, the size of the features causing the scattering is inversely proportional to q, so the USANS measurements allow scattering from larger, micrometer-scale features to be measured. For this work, the primary data of interest are obtained at the highest accessible q in the range of about 0.08–2.0 nm^{-1}. Scattering from hydrated cement paste in this q-range is dominated by the interface between the solid nanoscale C–S–H hydration product and the pore fluid, and it was anticipated that the same would be true for AAS paste. In general, the upper limit in q for obtaining data from hydrating cement is about 2 nm^{-1}, due to the decrease in SANS intensity with increasing q.

To perform composition and density analysis, one methanol-exchanged coupon and 4 water-saturated coupons of AAS paste cured for 28 days at 20°C were measured at the start of the experiment. They were then exchanged with a deuterated fluid. The methanol coupon was submerged in pure d3-methanol (CD_3OH). The water-saturated coupons were submerged in water containing 31%, 55%, 81%, and 100% D_2O (heavy water) by volume. The minimum exchange times were 24 h for the water-saturated coupons and 48 h for the methanol-saturated coupon. Each coupon was then measured a second time, taking care to expose the same location to the neutron beam. The SANS analysis of water content and mass density is based on the ratio of the SANS intensities obtained on the same coupons before and after exchange.

3. Results and discussion

3.1. General structural features of AAS paste

Fig. 1 shows combined SANS/USANS data for the AAS pastes. Such scattering curves are directly related to the underlying material microstructure over the length scale accessed, which in this case is approximately 1 nm to 10 μm. The datasets in Fig. 1 overlay each other closely and cannot be distinguished within the error of the measurements, which indicates that the micro- and nanostructure of AAS paste is essentially independent of curing time and temperature within the range tested. This is rather surprising as differences in curing temperature have significant microstructural effects on portland cement paste [18,19] that can be quantified with SANS [20].

For the AAS pastes shown in Fig. 1, the data exhibit a power-law (linear) slope close to −4 at lower q values where the scattering arises from larger, micrometer-scale features. This can be interpreted as Porod scattering arising from the surfaces of the cores of the unreacted slag particles. At higher q the intensity increases above the q^{-4} trend line, indicating scattering from nanoscale hydration product that is much finer than the original slag particles.

Fig. 2 shows the high-q data from one AAS paste replotted as Iq^4 vs. q, a format that enhances differences between related cement

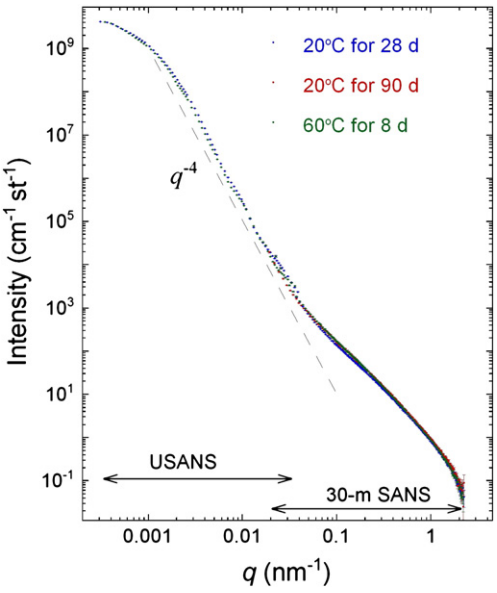

Fig. 1. SANS data for AAS pastes obtained from both USANS and 30-m SANS instruments. USANS data for the 90 days specimen are missing. The dashed line with slope of −4 is a guide to the eye indicating Porod scattering at lower q from unhydrated slag particles. Scattering at higher q arises from nanoscale hydration product, primarily C–S–H.

datasets. Also plotted for comparison are data from an ordinary portland cement (OPC) paste hydrated under the same conditions. The OPC dataset shows two distinct power-law regimes that have previously been interpreted as surface fractal scattering (at lower q) associated with the deposition of hydration product onto the hydrating cement particles, and volume fractal scattering associated with the fine nansocale C–S–H structure [21-23]. The AAS paste shows no evidence of surface fractal scattering. The significantly higher intensity of the AAS paste as compared to the OPC paste is due both to a greater amount of fine C–S–H product in the AAS paste and to different scattering contrast factors; this is discussed in Section 3.3.

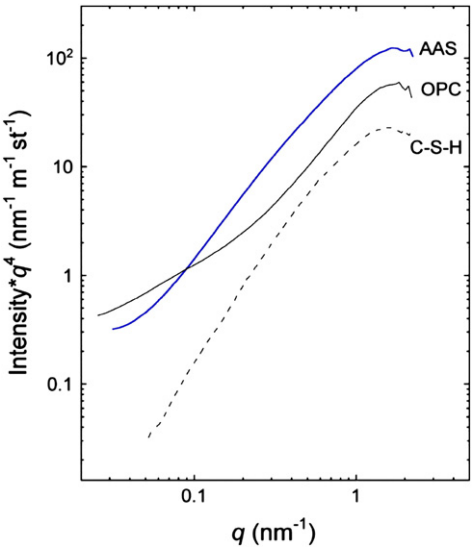

Fig. 2. SANS data for AAS and OPC pastes hydrated at 20 °C for 28 days and for a pure C–S–H gel. Only the high-q data representing scattering from nanoscale hydration product is shown. The OPC paste exhibits two power law regimes resulting from surface fractal and volume fractal scaling. The AAS paste does not exhibit surface fractal scattering, and the overall response is quite similar to that of pure C–S–H with a similarly low C/S of 1.0. The change in slope of the AAS data at lowest q is a transition to the Porod scattering from unhydrated particle cores (see Fig. 1).

This shape of the AAS dataset is quite similar to that of pure C–S–H gel with C/S = 1 formed by precipitation from solution, also plotted in Fig. 2. C–S–H formed by this method is chemically and structurally similar to C–S–H gel hydration product, as evidenced by the fact that it accelerates the hydration of both portland cement [24] and AAS paste [25] through a nucleation seeding effect. The pure gel has no large features that could generate surface fractal scattering. Overall, the SANS response from the AAS paste over the full SANS/USANS q-range suggests a structure consisting of unhydrated particle cores embedded in a relatively uniform matrix of nanoscale hydration product. This interpretation is in agreement with SEM images of AAS paste, e.g. [26,27].

3.2. Fluid exchange experiments

Determination of the mass density and water content (H/S) of the nanoscale solid C–S–H phase within a specimen requires calculating both the H_2O/D_2O contrast matchpoint and the neutron scattering length density, ρ, of the C–S–H phase; the latter is also required to calculate the specific surface area per unit volume from the SANS data. The experimental and analytical method for determining these parameters is discussed in detail in recent publications [16,28], so only an overview is given here. The contrast matchpoint for a solid phase in contact with a fluid is defined as the proportion of the fluid that must be in deuterated form, expressed as a volume fraction of the fluid, so that the scattering contrast is zero because the neutron scattering length densities of the solid and fluid phases are equal. Because ρ_{H2O} is actually negative ($-0.561\times10^{14}\,m^{-2}$), and ρ_{D2O} is strongly positive ($6.402\times10^{14}\,m^{-2}$), nearly all solid phases in contact with water have such a matchpoint.

For a two-phase system consisting of a single compositionally uniform solid phase and a fluid, a plot of the SANS intensity vs. the deuterated content of the fluid will be a parabola with a minimum of zero at the matchpoint. For a cement or tricalcium silicate paste, the scattering is dominated by the C–S–H–water interface, but even at the highest accessible q values corresponding to scattering from features a few nm in size there is also a small (a few percent) contribution from nanoscale CH [29,16]. As a result the relationship is parabolic but the minimum intensity is nonzero. These data can be fit as the sum of two parabolas representing CH and C–S–H.

While AAS pastes do not contain calcium hydroxide, the possibility that other phases such as hydrotalcite contribute to the high-q SANS intensity must be considered. Fig. 3 shows the experimentally determined contrast curve for the AAS paste cured at 20°C, along

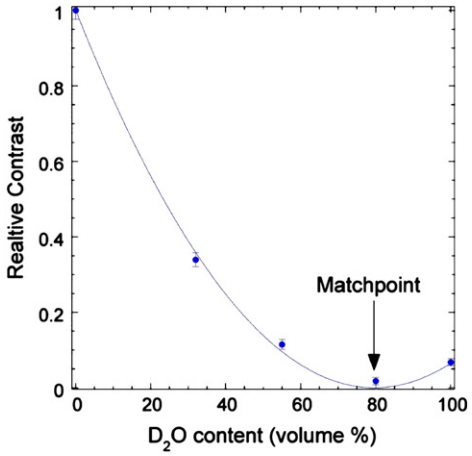

Fig. 3. Contrast curve for AAS paste hydrated for 28 d**ays** at 20 °C. The solid circles are the intensity of the high-q scattering at various D_2O contents, normalized by the intensity in pure H_2O, with measured standard deviation uncertainties shown as vertical bars. The line is a parabolic fit associated with the scattering from the interface between nanoscale solid C–S–H and the fluid.

with a single-parabola fit. The quality of the fit obtained with two parabolas (not shown) was not better than the fit obtained with a single parabola, indicating that the highest-q scattering is dominated by the C–S–H phase. The contrast matchpoint, determined from the fit shown in Fig. 3, occurs at $(79.7 \pm 1.0)\%$ volume D_2O.

When a thin paste specimen is exposed to an H_2O/D_2O mixture, all of the hydrogen in the solid C–S–H exchanges with the fluid [16], so the C–S–H takes on the same deuterated fraction as the fluid. To determine ρ_{CSH} (i.e., with only H and no D) requires exchanging with a fluid that only exchanges with the pore fluid and not with the solid phase. Deuterated methanol with composition CD_3OH is such a fluid, as the deuterated alcohol molecules cannot penetrate the solid C–S–H [16]. In this case, the scattering length density of the solid hydration product, ρ_{solid}, can be determined from [16,28]

$$\rho_{solid} = \frac{\rho_{CD_3OH}\sqrt{R} + \rho_{CH_3OH}}{1 + \sqrt{R}} \quad (1)$$

where R is the ratio of the SANS intensities in pure CH_3OH and pure CD_3OH for the same specimen and ρ_{solid} is the scattering length density of the nanoscale solid phase or phases. Fig. 4 shows the calculated value of ρ_{solid} as a function of q for the AAS paste. At higher q-values the ρ_{solid} value reaches a constant value of $(3.07 \pm 0.02) \times 10^{14}\ m^{-2}$. For cement pastes that have a scattering contribution from CH in this q-range, the value of ρ_{CSH} is slightly different from ρ_{solid} and is calculated using the parabolic contrast matchpoint fits [16]. However, for the present AAS specimen the high-q scattering is dominated by C–S–H, so $\rho_{CSH} = \rho_{solid}$. The scattering length density of fully deuterated C–S–D can also be calculated from ρ_{CSH} and the matchpoint [28]; this value is $\rho_{CSD} = (5.48 \pm 0.03) \times 10^{14}\,m^{-2}$.

A useful aspect of the fluid exchange experiments is that they allow the relative contributions of different phases to the scattered intensity to be determined. In an AAS paste, the dominant hydration products are C–S–H gel with the characteristics as determined above, and a hydrotalcite-type phase (assumed to be M_5AH_{13}). Fig. 5 shows the effects of fluid exchange with D_2O and 32 vol% D_2O. (Due to time constraints, these specimens were measured over a more limited q-range). The renormalization adjusts for the decreased contrast with C–S–H in these fluids, effectively ignoring any contribution from M_5AH_{13}. For the 32% D_2O dataset, the renormalized data lies on top of the original dataset, leading to the important conclusion that the hydrotalcite-type phase does not contribute to the nanoscale scattered intensity in the H_2O-saturated AAS paste. For the D_2O dataset, the renormalized data deviates above the original dataset. This

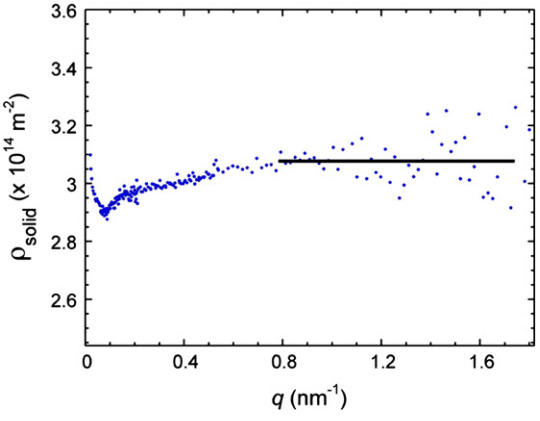

Fig. 4. Scattering length density of the nanoscale solid hydration product, ρ_{solid}, for the AAS paste. At each q value, ρ_{solid} is calculated from the ratio of the SANS intensities in CH_3OH and in CD_3OH according to Eq. (1). The scatter in the data reflects the uncertainties in the individual values. At higher q-values (corresponding to finer microstructural features) the calculated values become statistically constant as indicated by the horizontal line.

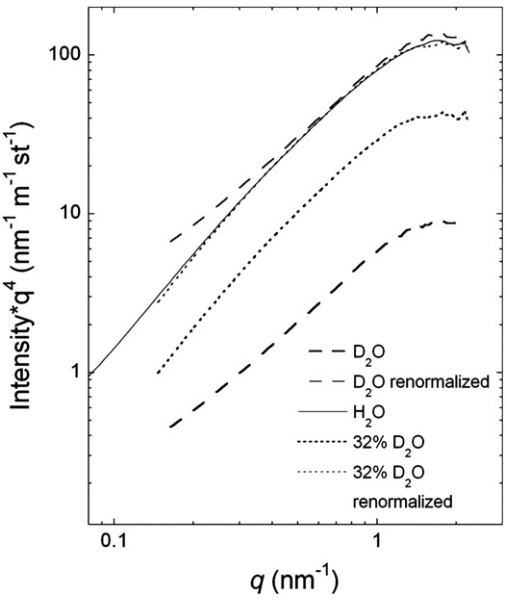

Fig. 5. Effect of fluid exchange with D_2O and 32 vol% D_2O on the SANS data from AAS paste. The scaling factors for renormalization are 2.79 (32 vol% D_2O) and 15.4 (D_2O). See text for more details.

confirms that hydrotalcite (or some other secondary phase) is indeed present in AAS paste, but only makes a significant contribution to the overall scattered intensity if its contrast is enhanced relative to that of C–S–H. The observed deviation between the H_2O and D_2O datasets only becomes significant at lower q values, indicating that the hydrotalcite phase is coarser than the C–S–H gel, although still possessing nanoscale structure.

It is difficult to predict *a priori* how much of the hydrogen in the hydrotalcite phase exchanges with D_2O. One reasonable scenario, which accounts for the above observation that the hydrotalcite contribution to the scattering is enhanced by exchange with pure D_2O, is that the four H_2O molecules per formula unit exchange with D_2O, while the hydrogen present in the form of bound hydroxyl groups (equivalent to nine water molecules per formula unit) does not exchange. With this assumption, exchange with pure D_2O will increase the contrast with M_5AH_{13} by a factor of about 3, while it decreases the C–S–H contrast by a factor of 15. Thus the relative contribution of M_5AH_{13} to the observed scattering would be increased by more than a factor of 60. For exchange with 32 vol% D_2O, the net effect is the opposite, such that the relative contribution of M_5AH_{13} would be decreased by more than a factor of 20.

3.3. Specific surface area of the AAS pastes

When a Porod scattering regime is observed in SANS data, then the specific surface area per unit specimen volume, S_T, associated with the relevant scattering features can be determined from:

$$S_T = \frac{C_P}{2\pi|\Delta\rho|^2} \quad (2)$$

where C_P is the constant of proportionality between I and q^{-4} for the Porod scattering regime and $|\Delta\rho|^2$ is the neutron scattering contrast factor. The contrast factor is the square of the difference in the neutron scattering length densities of the phases generating the Porod scattering, and it defines the inherent intensity of the scattering from the interface between these phases. For a saturated cementitious material, the appropriate contrast factor for Eq. (2) is $(\rho_{solid} - \rho_{H2O})^2$. For AAS pastes the value of ρ_{solid} was determined in the previous section and the scattering contrast factor is $(13.2 \pm 0.1) \times 10^{28}\,m^{-4}$. This is 35% higher than

the measured contrast factor for portland cement or C_3S pastes [16]. This higher contrast explains some, but not all, of the higher intensity of the AAS paste relative to the OPC paste in Fig. 2.

Surface area values for the AAS pastes are given in Table 2, along with previously reported values for OPC, white portland cement (WPC) and C_3S pastes hydrated under similar conditions. The S_T values for AAS increase moderately with curing time between 8 days and 3 months, and the values, even at 8 days of curing, are higher than all measured S_T values for cement or C_3S paste. The higher S_T of the AAS pastes is likely related to the development of a low-density C–S–H phase that fills the pore space. The S_T value of C_3S paste is increased by both $CaCl_2$ acceleration [24] and by seeding with C–S–H [23], and both of these additives increase the amount of low-density C–S–H visible in micrographs.

3.4. Estimation of the C/S and A/S molar ratios of C–S–H

Chen and Brouwers [15] presented a stoichiometric model for hydration of AAS that calculates the quantities of the hydration products and the composition of the C–S–H based on the mole percentages of the main oxide constituents of the unhydrated slag and activator. Their model predicts the C/S and A/S values of the C–S–H, which are the values needed for the present study. The model assumes that all of the magnesium forms a hydrotalcite-type phase (M_5AH_{13}), all of the iron forms hydrogarnet ($C_6AFS_2H_8$), and all of the sulfur forms ettringite ($C_6A\bar{S}_3H_{32}$). The remaining calcium, aluminum, and silicon enter the C–S–H phase and, possibly, AFm phases (either C_4AH_{13} or C_2ASH_8).

To model aluminum substitution into C–S–H in AAS pastes, Chen and Brouwers adopted the following linear relationship, developed originally by Richardson [32], to define the maximum allowable aluminum substitution:

$$A/S = \frac{1 - 0.4277(C/S)}{4.732} \tag{3}$$

With slags that are high in aluminum or low in magnesium, the A/S of the C–S–H takes on the maximum value given by Eq. (3) and the remaining aluminum enters an AFm phase. With slags that are low in aluminum or high in magnesium, the substitution limit is not reached so all remaining aluminum enters the C–S–H and AFm does not form. Chen and Brouwers tested their model against three published experimental studies of AAS [33-35] and found it to give predicted C/S and A/S values in good agreement with the experimentally measured values reported from those studies.

The Chen and Brouwers model [15] was applied to the AAS used in the present study, using the oxide mole percentages listed in Table 1 (right column). The predictions of the model are given in Table 3. The phase composition of the hydrated AAS paste is dominated by the C–S–H phase, in agreement with experimental observations [33-35]. The degree of aluminum substitution is fairly low ($A/S = 0.06 \pm 0.01$) so no AFm phase forms.

Table 2
SANS specific surface areas of AAS pastes, along with previously published SANS values for other paste types.

Paste type	ref	S_T (m^2/cm^3)
AAS 20 °C 28 days	this work	148(7)[a]
AAS 20 °C 90 days	this work	173(9)
AAS 60 °C 8 days	this work	153(8)
OPC 20 °C[b]	[30,31]	95–132
C_3S 20C[b]	[23,29]	105–120
WPC 20C[b]	[20,22,29]	110–135

[a] The numbers in parentheses are estimated uncertainties in least significant digits.
[b] Ages ranging from 8 days to 6 months, water/cement ratios 0.4 to 0.5.

Table 3
Predicted phase formation and C–S–H composition using the model of Chen and Brouwers [15].

Phase	mole%
C–S–H	90.9(10)[a]
M_5AH_{13}	7.6(1)
$C_6AFS_2H_8$	0.4(1)
$C_6A\bar{S}_3H_{32}$	1.1(2)
Total	100
C/S (C–S–H)	0.99(2)
A/S (C–S–H)	0.06(1)

[a] The numbers in parentheses are calculated standard deviations in least significant digits.

3.5. Mass density and water content of the solid nanoscale C–S–H

The predicted C–S–H composition in the AAS paste (see Table 3) is $C_{0.99}$–S–$A_{0.06}$–H_y, where $y = H/S$ is the water content, which can vary depending on how the phase is defined and on the drying state. One useful definition of H/S is the water content of the solid nanoscale C–S–H, which includes hydroxyl groups and H_2O held in the interlayer space but excludes any adsorbed or gel pore water. This solid H/S value represents the composition of the solid C–S–H that scatters against the pore fluid in a SANS experiment, and it also represents the water that does not exchange with methanol.

Once the composition of the other components of the C–S–H is known (C/S and A/S) then the solid H/S and the associated mass density can be calculated from the equations defining the neutron scattering length densities, ρ_{CSH} and ρ_{CSD}:

$$\rho_{CSH} = \frac{(C/S)b_{CaO} + b_{SiO_2} + (A/S)b_{Al_2O_3} + (H/S)b_{H_2O}}{MW_{CSH}} N_A d_{CSH} \tag{4}$$

and

$$\rho_{CSD} = \frac{(C/S)b_{CaO} + b_{SiO_2} + (A/S)b_{Al_2O_3} + (H/S)b_{D_2O}}{MW_{CSH}} N_A d_{CSH} \tag{5}$$

where b_{CaO} is the established neutron scattering length of CaO, etc., MW_{CSH} is the molar mass of C–S–H, N_A is Avagadro's number, and d_{CSH} is the mass density of C–S–H. The form of Eq. (5) utilizes the fact that substituting D for H in a phase affects the molar mass and mass density equally. Since the values of ρ_{CSH} and ρ_{CSD} were determined experimentally (see Section 3.2), Eqs. (4) and (5) have only H/S and d_{CSH} as unknowns, and thus these parameters can be solved for. The resulting values are: $H/S = (0.97 \pm 0.03)$ and $d_{CSH} = (2.73 \pm 0.02)$ g/cm^3, and the molar volume is (50.8 ± 0.6) cm^3.

To put these values into context, it is useful to compare them to the measured composition and molar volume of normal C–S–H formed in portland cement or C_3S paste ($C_{1.7}$–S–$H_{1.8}$, MV = 72.1 cm^3 [16]). Recently, we presented a method of comparing the atomic packing density of various calcium silicate hydrate phases by comparing the molar volumes at equivalent compositions [28]. That study concluded that the atomic packing density of solid nanoscale C–S–H gel is significantly higher than that of related minerals such as tobermorite or jennite. In the present case, the appropriate amounts of CaO and solid H_2O are added to the AAS C–S–H, and the Al_2O_3 is subtracted, to reach the composition noted above for normal C–S–H. The molar volume of this hypothetical phase mixture is (74.8 ± 1.1) cm^3, which is slightly larger (by 4%) than the molar volume of normal C–S–H. This indicates that the atomic packing of AAS C–S–H is slightly lower than that of normal C–S–H, despite its higher mass density. On the other hand, when the composition of the AAS C–S–H is adjusted by the same method to match the composition of 1.1 nm tobermorite, which has a much more similar composition ($C_{0.75}$–S–$H_{0.93}$, MV = 47.9 cm^3), the result is a molar volume of (44.5 ± 0.6) cm^3,

which is 12% lower than that of 1.1 nm tobermorite. This indicates that the atomic packing of the AAS C–S–H is significantly greater than that of tobermorite, despite the similarity in compositions.

Because the values reported here are for one particular AAS paste, it is useful to estimate their sensitivity to changes in the AAS composition, as this will vary somewhat depending on the particular slag and activator used. In general, the H/S and C/S of C–S–H tend to vary together due to the details of its atomic structure [36], and changes in the H/S and C/S in the same direction will have counteracting effects on the mass density. As an illustration, note that while the H/S and C/S of the AAS paste are each only about half the values measured for normal C–S–H gel, the measured density values for these phases differ by less than 5%. A similar effect occurs with the neutron scattering length density. Due to the much higher neutron scattering cross section of hydrogen as compared to other elements, the measured value of ρ_{CSH} will depend, as a first approximation, on the molar ratio of water to the total of the other elements, H/(C + S + A). Thus we conclude that while the composition of AAS will vary from paste to paste, the C–S–H scattering length density, scattering contrast, and solid mass density will vary much less, and the values determined here would not result in much error if used for AAS pastes in general.

3.6. Chemical shrinkage

Chemical shrinkage, which is defined as the decrease in the total volume of the paste components as hydration proceeds, is an important property of cementitious materials as it can lead to the formation of internal stresses and cracking even when a specimen is cured under water [5,25]. The primary effect of chemical shrinkage is migration of water within the pore system, with larger pores emptying to supply water for the hydration reactions. If this water is not replenished, then this pore emptying results in internal capillary stresses. For a paste in contact with a reservoir of water, the uptake of water into the specimen can be used to measure the chemical shrinkage over time [37], as long as the pore structure remains connected so the sample does not self-desiccate.

To calculate the chemical shrinkage of a paste requires knowing the composition and molar volume of the water-saturated C–S–H phase, but this parameter has historically proven difficult to determine. However, the values obtained for solid C–S–H from the neutron scattering exchange method allow an accurate estimate to be made, as the only additional step that is needed is to estimate the amount of adsorbed water associated with C–S–H and its effective density or molar volume. For C–S–H with the C/S value of 1.7 associated with normal portland cement paste, we recently estimated that the chemical shrinkage of cement paste cured at room temperature would be in the range of 5–6 cm^3/100 g (volumetric decrease per mass of unhydrated cement), depending on the cement mineral composition [28], in good agreement with measured values [37,38]. For that calculation, each mole of C–S–H was assumed to have 0.3 moles of adsorbed water with density 1.1 g/cm^3 and any additional water was assumed to be bulk water that does not change its effective density during hydration. A similar estimation of the chemical shrinkage of the AAS paste from this work (see Table 4) yields a value of (12.2 ± 1.5) cm^3/100 g, which is about twice the value of portland cement. Note that the uncertainty on this value accounts only for the uncertainty in the composition and density of the hydrated phases and unhydrated slag, and does not account for any uncertainty in the volume fractions of the phases resulting from the use of the hydration model of ref. [15].

To our knowledge the chemical shrinkage of AAS has not been measured directly. Such a measurement would be difficult, due to the onset of self-desiccation and associated autogeneous shrinkage at very early times [6,25]. Chen and Brouwers [15] calculated the chemical shrinkage of AAS paste using a method similar to that shown in Table 4, resulting in comparable values in the range of 11.5–14 cm^3/100 g. Bentz [39] quoted a higher chemical shrinkage value (18 cm^3/100 g) for hydration of slag based on unpublished results, but details were not given. As discussed in the previous section, our results indicate that the atomic packing density of AAS C–S–H is slightly lower than that of normal C–S–H, which would tend to give a lower chemical shrinkage. Thus the large chemical shrinkage associated with AAS hydration is likely related to the glassy nature of the slag itself, which results in a relatively low atomic packing density of the unhydrated material.

Table 4
Calculation of chemical shrinkage for AAS hydration.

Products[a]	moles	d (g/cm^3)	volume (cm^3)
C–S–H	0.631	2.73	32.1(6)[b]
H_2O (adsorbed)	0.189	1.1	3.1(5)
M_5AH_{13}	0.053	1.99	14.3(9)
$C_6AFS_2H_8$	0.003	3.03	0.9(4)
$C_6A\bar{S}_3H_{32}$	0.007	1.78	5.2(6)
Total	-	-	55.5(16)
Ingredients[a]	**moles**	**d (g/cm^3)**	**volume (cm^3)**
Slag (100 g)	-	2.90	34.5(3)
SiO_2	0.062	2.20	1.70(1)
H_2O[c]	1.748	1.00	31.5
Total	-	-	67.6(3)
Chemical shrinkage	-	-	12.2(15) cm^3/100 g

[a] Composition of products and ingredients, including H_2O, is identical.
[b] The numbers in parentheses are calculated uncertainties in least significant digits.
[c] Portion of mix water that is bound onto hydration products.

AAS paste is more prone to cracking than portland cement, even when it is not permitted to dry [5,25]. The present results and calculations support the hypothesis that this is due in part to the greater chemical shrinkage of AAS paste. The effects of chemical shrinkage may be exacerbated by the fact that AAS pastes form with a lower permeability, which prevents water from reaching the interior of specimens during saturated (under water) curing, leading to differential stresses that can cause cracking [25].

4. Conclusions

AAS paste activated with sodium silicate was analyzed using SANS and USANS, allowing the scattering from features ranging in size from about 1 nm to a few μm to be measured. The qualitative interpretation of the scattering response is of a rather uniform matrix of nanoscale hydration product studded with unhydrated cores of slag particles. This is quite different from the response from a portland cement paste, which exhibits surface fractal scattering associated with deposition of denser hydration product around the reacting grains. An interesting result is that elevated temperature curing at 60°C had no effect on the scattering response, and thus on the microstructure. The specific surface area of the AAS pastes is about 25% higher than that of a portland cement paste cured under the same conditions.

The composition and mass density of the C–S–H phase formed in the AAS paste was determined in two separate steps. The C/S ratio and degree of Al substitution (C/S = 0.99 ± 0.2, A/S = 0.06 ± 0.01) were calculated from the composition of the slag and activator using a hydration model developed and verified by Chen and Brouwers [15]. The water content and mass density of the C–S–H (H/S = 0.97 ± 0.03, d = 2.73 ± 0.02 g/cm^3) were determined experimentally using the SANS-based contrast variation method developed previously by us [16]. As compared to the solid C–S–H formed in a normal portland cement paste, the C/S and H/S are considerably lower, while the mass density is slightly higher. The composition of the AAS C–S–H is similar to that of 1.1 nm tobermorite, but molar volume calculations indicate that the atomic packing density is significantly higher.

The C–S–H results given above were used to calculate the chemical shrinkage that would result from complete hydration of the AAS

paste. The result, $(12.2 \pm 1.5)\ cm^3/100\ g$, is about twice the amount of chemical shrinkage exhibited by portland cement paste.

Acknowledgments

This work utilized neutron scattering facilities supported in part by the National Science Foundation under Agreement No. DMR-0454672.

References

[1] V. Glukhovsky, Y. Zaitsev, V. Pakhomow, Slag-alkaline cements and concrete structures, properties, technologies, and economic aspects of their use, Silic. Indus. 10 (1983) 197–200.
[2] S.-D. Wang, X.C. Pu, K.S. Scrivener, P.L. Pratt, Alkali-activated slag cement and concrete: a review of properties and problems, Adv. Cem. Res. 7 (1995) 93–102.
[3] C. Li, H.H. Sun, L.T. Li, A review: the comparison between alkali-activated slag (Si plus Ca) and metakaolin (Si plus Al) cements, Cem. Concr. Res. 40 (2010) 1341–1349.
[4] M. Palacios, P.F.G. Banfill, F. Puertas, Rheology and setting of alkali-activated slag pastes and mortars: effect of organic admixture, ACI Mater. J. 105 (2008) 140–148.
[5] T. Hakkinen, The influence of slag content on the microstructure, permeability, and mechanical properties of concrete. Part 1. Microstructural studies and basic mechanical properties, Cem. Concr. Res. 23 (1993) 407–421.
[6] A.A. Melo Neto, M.A. Cincotto, W. Repette, Drying and autogenous shrinkage of pasted and mortars with activated slag cement, Cem. Concr. Res. 38 (2008) 565–574.
[7] C.D. Atis, C. Bilim, O. Celik, O. Karahan, Influence of activator on the strength and drying shrinkage of alkali-activated slag mortar, Constr. Build. Mater. 23 (2009) 548–555.
[8] F. Collins, J.G. Sanjayan, Cracking tendency of alkali activated slag subjected to restrained shrinkage, Cem. Concr. Res. 30 (2000) 791–798.
[9] T. Bakharev, J.G. Sanjayan, Y.B. Cheng, Effect of admixtures on properties of alkali-activated slag concrete, Cem. Concr. Res. 30 (2000) 1367–1374.
[10] M. Palacios, F. Puertas, Effect of shrinkage-reducing admixtures on the properties of alkali-activated slag mortars and pastes, Cem. Concr. Res. 37 (2007) 691–702.
[11] F. Collins, J.G. Sanjayan, Effect of pore size distribution on drying shrinkage of alkali-activated slag concrete, Cem. Concr. Res. 30 (2000) 1401–1406.
[12] I.G. Richardson, A.R. Brough, G.W. Groves, C.M. Dobson, The characterization of hardened alkali-activated blast-furnace slag pastes and the nature of the calcium silicate hydrate (C–S–H) phase, Cem. Concr. Res. 24 (1994) 813–829.
[13] S.-D. Wang, K.L. Scrivener, ^{29}Si and ^{27}Al NMR study of alkali-activated slag, Cem. Concr. Res. 33 (2003) 769–774.
[14] H.F.W. Taylor, Cement Chemistry, Thomas Telford, London, 1997.
[15] W. Chen, H.J.H. Brouwers, The hydration of slag, Part 1: Reaction models for alkali-activated slag, J. Mater. Sci. 42 (2007) 428–443.
[16] A.J. Allen, J.J. Thomas, H.M. Jennings, Composition and density of nanoscale calcium-silicate-hydrate in cement, Nat. Mater. 6 (2007) 311–316.
[17] Certain commercial materials and equipment are identified in this paper only to specify adequately the experimental procedure. In no case does such identification imply recommendation by NIST nor does it imply that the material or equipment identified is necessarily the best available for this purpose.
[18] A. Bentur, R.L. Berger, J.H. Kung, N.B. Milestone, J.F. Young, Structural properties of calcium silicate pastes: II, Effect of curing temperature, J. Am. Ceram. Soc. 62 (1979) 362–366.
[19] K.O. Kjellsen, R.J. Detwiler, O.E. Gjorv, Backscattered electron imaging of cement pastes hydrated at different temperatures, Cem. Concr. Res. 20 (1990) 308–311.
[20] H.M. Jennings, J.J. Thomas, J.S. Gevrenov, G. Constantinides, F.-J. Ulm, A multi-technique investigation of the nanoporosity of cement paste, Cem. Concr. Res. 37 (2007) 329–336.
[21] A.J. Allen, R.C. Oberthur, D. Pearson, P. Schofield, C.R. Wilding, Development of the fine porosity and gel structure of hydrating cement systems, Philos. Mag. B 56 (1987) 263–268.
[22] J.J. Thomas, A.J. Allen, H.M. Jennings, Structural changes to the calcium silicate hydrate gel phase of hydrated cement with age and on drying and resaturation, J. Am. Ceram. Soc. 91 (2008) 3362–3369.
[23] J.J. Thomas, A.J. Allen, H.M. Jennings, Hydration kinetics and microstructure development of normal and $CaCl_2$-accelerated tricalcium silicate (C_3S) pastes, J. Phys. Chem. C 113 (2009) 19836–19844.
[24] J.J. Thomas, H.M. Jennings, J.J. Chen, Influence of nucleation seeding on the hydration mechanisms of tricalcium silicate and cement, J. Phys. Chem. C 113 (2009) 4327–4334.
[25] M.H. Hubler, J.J. Thomas, H.M. Jennings, Influence of nucleation seeding on the hydration kinetics and compressive strength of alkali activated slag paste, Cem. Concr. Res. 41 (2011) 842–846.
[26] F. Puertas, A. Fernandez-Jimenez, M.T. Blanco-Varela, Pore solution in alkali-activated slag cement pastes. Relation to the composition and structure of calcium silicate hydrate, Cem. Concr. Res. 34 (2004) 139–148.
[27] I. Lecomte, C. Henrist, M. Liegeois, F. Maseri, A. Rulmont, R. Cloots, (Micro)-structural comparison between geopolymers, alkali-activated slag cement and portland cement, J. Eur. Ceram. Soc. 26 (2006) 3789–3797.
[28] J.J. Thomas, H.M. Jennings, A.J. Allen, Relationships between composition and density of tobemorite, jennite, and nanoscale $CaO–SiO_2–H_2O$, J. Phys. Chem. C 114 (2010) 7594–7601.
[29] J.J. Thomas, J.J. Chen, A.J. Allen, H.M. Jennings, Effects of decalcification on the microstructure and surface area of cement and tricalcium silicate pastes, Cem. Concr. Res. 34 (2004) 2297–2307.
[30] J.J. Thomas, H.M. Jennings, A.J. Allen, The surface area of cement paste as measured by neutron scattering—evidence for two C–S–H morphologies, Cem. Concr. Res. 28 (1998) 897–905.
[31] A.J. Allen, J.J. Thomas, Analysis of C–S–H gel and cement paste by small-angle neutron scattering, Cem. Concr. Res. 37 (2007) 319–324.
[32] I.G. Richardson, The nature of C–S–H in hardened cements, Cem. Concr. Res. 29 (1999) 1131–1147.
[33] I.G. Richardson, G.W. Groves, Microstructure and microanalysis of hardened cement pastes involving ground granulated blast-furnace slag, J. Mater. Sci. 27 (1992) 6204–6212.
[34] S.-D. Wang, K.L. Scrivener, Hydration products of alkali activated slag cement, Cem. Concr. Res. 25 (1995) 561–571.
[35] A.R. Brough, A. Atkinson, Sodium silicate-based alkali-activated slag mortars. Part 1: strength, hydration and microstructure, Cem. Concr. Res. 32 (2002) 865–879.
[36] J.J. Thomas, D.A. Neumann, J.J. Chen, H.M. Jennings, Ca–OH bonding in the C–S–H gel phase of tricalcium silicate and white portland cement pastes measured by inelastic neutron scattering, Chem. Mater. 15 (2003) 3813–3817.
[37] M. Geiker, T. Knudsen, Chemical shrinkage of portland cement pastes, Cem. Concr. Res. 12 (1982) 603–610.
[38] E. Tazawa, S. Miyazawa, T. Kasai, Chemical shrinkage and autogenous shrinkage of hydrating cement paste, Cem. Concr. Res. 25 (1995) 288–292.
[39] D.P. Bentz, Internal curing of high-performance blended cement mortars, ACI Mater. J. (July-August 2007) 408–414.